ROYAL SOCIETY
OF CHEMISTRY

## PAPER

Check for updates

# Catalytic metal-induced crystallization of sol–gel metal oxides for high-efficiency flexible perovskite solar cells†

Cheng-Hung Hou,[a] Jing-Jong Shyue, [ID][ab] Wei-Fang Su [ID][a] and Feng-Yu Tsai [ID]*[a]

Sol–gel metal oxide films are an important type of functional materials for energy technologies and beyond owing to their versatile properties and ease of processing, but their applications are limited by the typically required high sintering temperatures. This study reports a novel phenomenon where the sintering temperatures of sol–gel metal oxide films were substantially lowered when a metal phase was embedded within the sol–gel precursor films. Morphological and compositional analyses revealed that the reduction in sintering temperatures was enabled by a mechanism similar to the metal-induced crystallization (MIC) process, with a distinction that catalysis of sol–gel reactions occurred alongside the induction of crystallization. We observed this catalytic MIC (c-MIC) mechanism in a variety of sol–gel material systems including $Ni_xO$ with embedded Au or Ag; $TiO_x$ with embedded Ni, Au, or Pt; and $SnO_x$ with embedded Ni. Based upon this concept, we demonstrated highly efficient flexible and rigid organic/inorganic hybrid perovskite solar cells (PSCs) using a low-temperature-sintered $Ni_xO$ film embedded with Au nanoislands as the hole-transporting layer (HTL). The c-MIC mechanism reduced the sintering temperature of the Au-embedded $Ni_xO$ HTL by 100 °C, making the $Ni_xO$ process compatible with plastic substrates while allowing the $Ni_xO$ HTL to retain more NiOOH surface groups, which enhanced hole collection and improved the quality of the perovskite layer. Thanks to the advantages of the c-MIC $Ni_xO$ film, the flexible and rigid PSCs achieved high power conversion efficiencies of up to 15.9 and 19.0%, respectively, which were sustained for >1200 h at 65 °C and 65% relative humidity. Our findings provide a practical route for low-temperature fabrication of high-quality oxide functional films by solution-based sol–gel processes, which will be valuable to a wide variety of applications in addition to thin film solar cells.

## Introduction

Thanks to their versatile yet excellent properties, metal oxide functional materials are indispensable in almost all types of existing and upcoming energy applications, from energy generation technologies such as solar cells[1–3] and thermoelectric generators,[4–6] energy storage technologies such as batteries[6–9] and supercapacitors,[6,10,11] to energy conservation technologies such as light-emitting diodes[12,13] and transistors/sensors[14,15] used in smart appliances. Additionally, many metal oxides can be cast into films *via* solution-based sol–gel processes, which greatly enhance their manufacturability over the commonly used vacuum deposition techniques. However, the sol–gel process of metal oxide films still poses significant challenges that limit their practical application. Firstly, the sol–gel process typically requires a high-temperature sintering step to thoroughly remove

the organic contents contained in the reaction chemistry, but the random and explosive escaping patterns of the organic contents at such high temperatures often lead to non-uniform, defect-laden films. Secondly, the high sintering temperatures, also required to obtain adequate crystallinity from crystalline metal oxides, render many sol–gel chemistries incompatible with sensitive materials such as organic semiconductors and plastic substrates. Moreover, the energy- and cost-intensiveness of the high-temperature process undermines the merits of sol–gel metal oxides in energy-related applications. Recent research has demonstrated low-temperature fabrication of metal oxide films by casting from metal-oxide nano-crystal suspension solutions[16] or by combustion sol–gel reactions.[14,17,18] Such methods, however, still face limitations in that casting from a nanocrystal solution tends to leave copious discontinuities in the resultant film, and the organic fuels required in the combustion method can produce large amounts of escaping side products, forming voids and defects in the resultant film. Consequently, a sol–gel method that can achieve thorough chemical conversion, adequate crystallization, and good film quality in metal oxide functional materials without the need of a high-temperature sintering step will be highly valuable.

[a]*Department of Materials Science and Engineering, National Taiwan University, No. 1, Sec. 4, Roosevelt Rd., Taipei, 10617, Taiwan. E-mail: ftsai@ntu.edu.tw*

[b]*Research Center of Applied Science, Academia Sinica, Taipei, 11529, Taiwan*

† Electronic supplementary information (ESI) available: Details of materials synthesis, device fabrication and characterisation. See DOI: 10.1039/c8ta05973j

In this study, we discovered a novel phenomenon related to the metal-induced crystallization (MIC) mechanism,[19–24] where the sintering temperatures of sol–gel metal oxide films were greatly reduced when a metal phase was embedded within the sol–gel precursors. The discovery was serendipitous during an attempt to incorporate a $Ni_xO$ hole-transporting layer (HTL) into hybrid organic–inorganic perovskite solar cells (PSCs) to take advantage of the excellent electron-blocking/hole-transporting function and the environmental stability of $Ni_xO$.[25–31] Upon observing that the optimal sintering temperature of the $Ni_xO$ HTL—in terms of the PSC device performance—was lowered by 100 °C when an Au phase (in the form of nanoislands or a film) was embedded in it, we conducted a series of microstructural and compositional analyses on the $Ni_xO$ films, with which we determined that the reduction in the sintering temperature was via a MIC-like mechanism. We verified such a mechanism, which we termed catalytic MIC (c-MIC), occurred in a variety of other sol–gel material systems, including $TiO_x$ with embedded Ni, Au, or Pt; $SnO_x$ with embedded Ni; and $NiO_x$ with embedded Ag instead of Au. Finally, utilizing the low-temperature sintering process of the Au-embedded $Ni_xO$ HTL, we demonstrated high-efficiency flexible and rigid PSC devices with excellent environmental stability as an example of the utility of the c-MIC mechanism in energy applications.

## Results and discussion

The first manifestation of the c-MIC phenomenon that we observed was the significant reduction in the optimal sintering temperature of a $Ni_xO$ HTL, in terms of PSC performance and crystallinity, when the $Ni_xO$ HTL was embedded with Au nanoislands. The device characteristic of the PSCs with a regular $Ni_xO$ HTL (no embedded Au phase) or the Au-embedded $Ni_xO$ HTL sintered at various temperatures are compared in Table 1, Fig. 1a and b. The embedded Au phase was in the form of nanoislands, which was prepared by reflowing a thermally evaporated 1 nm-thick Au film by thermal annealing (30 min at 150 °C). The Au nanoislands were roughly in the shape of thin circular plates with ∼5–10 nm diameters, as shown in Fig. S2 (ESI†). The Au nanoislands were highly transparent to UV-visible light except for the wavelength range centered at ∼550 nm, where absorption owing to localized surface plasmon resonance (LSPR) effects of the Au nanoislands reduced the optical transmission into the PSC devices by 3–10%, as shown in Fig. S3 (ESI†).

With the regular $Ni_xO$ HTL (Table 1 and Fig. 1a), a 180 °C sintering temperature resulted in poor PSC performance, where the high series resistance ($R_s$), low short-circuit current density ($J_{sc}$) and low open-circuit voltage ($V_{oc}$) pointed to low hole mobility and the presence of impurity in the $Ni_xO$ HTL due to

**Table 1** Device metrics of PSCs under different $Ni_xO$ sintering conditions, where Au/$Ni_xO$ denotes Au nanoisland-embedded $Ni_xO$ films. The error bars were 95% confidence intervals calculated from 10 devices each fabricated from a different run. Box plots of the PCE values of all the devices are shown in Fig. S1 (ESI)

| HTL | $V_{oc}$ (V) | $J_{sc}$ (mA cm$^{-2}$) | FF (%) | PCE (%) | $R_s{}^a$ (Ω cm$^2$) |
|---|---|---|---|---|---|
| $Ni_xO$-300 °C | 1.03 ± 0.02 | 20.0 ± 1.4 | 66.3 ± 2.8 | 13.7 ± 0.8 | 9.4 ± 1.6 |
| $Ni_xO$-280 °C | 1.04 ± 0.01 | 21.7 ± 0.3 | 70.1 ± 3.2 | 16.1 ± 0.8 | 6.7 ± 1.2 |
| $Ni_xO$-240 °C | 1.05 ± 0.02 | 20.5 ± 1.4 | 65.6 ± 5.6 | 13.8 ± 0.9 | 10.4 ± 4.5 |
| $Ni_xO$-200 °C | 0.90 ± 0.09 | 19.7 ± 2.1 | 58.4 ± 5.5 | 11.1 ± 1.2 | 13.8 ± 5.4 |
| $Ni_xO$-180 °C | 0.88 ± 0.09 | 13.6 ± 4.6 | 57.9 ± 8.0 | 6.9 ± 2.5 | 15.9 ± 8.0 |
| Au/$Ni_xO$-200 °C | 1.04 ± 0.01 | 21.2 ± 1.0 | 74.6 ± 2.2 | 16.4 ± 0.9 | 5.3 ± 1.3 |
| Au/$Ni_xO$-180 °C | 1.04 ± 0.01 | 22.2 ± 0.3 | 78.0 ± 3.5 | 17.9 ± 0.8 | 4.3 ± 1.6 |
| Au/$Ni_xO$-160 °C | 0.87 ± 0.11 | 15.2 ± 2.5 | 54.7 ± 11.3 | 7.3 ± 2.2 | 14.5 ± 4.1 |

[a] Series resistances ($R_s$) were determined by taking the reciprocal values of the J–V slopes under open-circuit conditions.
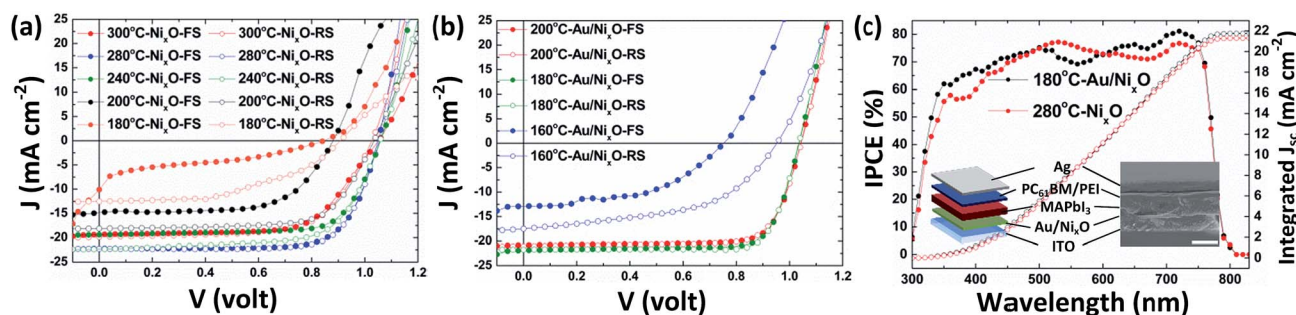


**Fig. 1** J–V curves of PSCs with (a) regular $Ni_xO$ HTL and (b) Au nanoisland-embedded $Ni_xO$ HTL sintered at various temperatures. The results obtained from the forward scan (solid circles) and the reverse scan (empty circles) are both presented for the examination of J–V hysteresis; (c) IPCE spectra and integrated $J_{sc}$ curves of devices with optimally sintered Au nanoisland-embedded $Ni_xO$ HTL and $Ni_xO$ HTL. The inset in (c) shows the device architecture and cross-section SEM image of the PSC device.

This journal is © The Royal Society of Chemistry 2018

J. Mater. Chem. A, 2018, 6, 16450–16457 | 16451

incomplete sintering.[32] Moreover, the PSC devices exhibited severe $J$–$V$ hysteresis, as shown by the pronounced difference between the forward-scan (FS) and reverse-scan (RS) $J$–$V$ curves, indicating the abundance of hysteresis-inducing charge-trapping defects in the $Ni_xO$ HTL.[33,34] Incrementally raising the sintering temperature gradually improved the PSC device performance and $J$–$V$ hysteresis until 280 °C, above which the performance started to decline due to degradation in the conductivity of the ITO electrode. The highest average power conversion efficiency (PCE) of the PSC devices, 16.1%, was obtained with a sintering temperature of 280 °C, where the $J$–$V$ hysteresis was also eliminated (*i.e.* identical FS and RS $J$–$V$ curves). Analysis with grazing incidence X-ray diffraction (GIXRD) revealed that the crystallinity evolution of the $Ni_xO$ HTL at various sintering temperatures correlated well with the PSC performance results. As shown in Fig. S4 (ESI†), the 180 °C-sintered $Ni_xO$ films were essentially amorphous, showing no observable diffraction peak. The NiO characteristic diffraction peaks—at 35.7°, 43.1°, and 62.7°, corresponding to the (111), (200), and (220) planes, respectively—started to appear as the sintering temperature increased to 200 °C, and they gradually intensified with higher sintering temperatures until 280 °C, above which the peak intensities remained unchanged. Both the PSC device and GIXRD results indicated that for the regular $Ni_xO$ HTL to be fully sintered, the sintering temperature should be at least 280 °C.

With the Au-embedded $Ni_xO$ HTL, in contrast, the sintering temperature required for the PSC devices to achieve optimal performance was only 180 °C. While the Au-embedded $Ni_xO$ HTL appeared to be incompletely sintered at 160 °C, as evidenced by the high $R_s$, low $J_{sc}$, low $V_{oc}$, and severe $J$–$V$ hysteresis of the corresponding PSC devices, sintering was apparently

complete at 180 °C, where all of the device characteristics were significantly improved, leading to the optimal average PCE of 17.9% (19.0% champion) and elimination of $J$–$V$ hysteresis. Further increasing the sintering temperature to 200 °C did not further improve the PSC device performance but caused slight deterioration (discussed later). The accuracy of the measured device metrics of the optimal with- (180 °C-annealed) and without-Au (280 °C-annealed) PSC devices was verified with incident photon-to-current efficiency (IPCE) measurements, as shown in Fig. 1c, where the integrated photo-current density of the two devices across the incident light spectrum agreed well with their $J_{sc}$ values measured with the solar simulator.

Microstructural analyses also revealed that the 180 °C-sintering of the Au-embedded $Ni_xO$ HTL resulted in extensive crystallinity. We first conducted GIXRD analysis, which showed strong diffraction peaks at 35.7°, 43.1°, and 62.7° in the 180 °C-sintered Au-embedded $Ni_xO$ HTL, as shown in Fig. S5 (ESI†). However, this was not adequate evidence of the crystallinity of the $Ni_xO$ HTLs, as the three diffraction peaks correspond to both the NiO (JCPDS 47-1049) and the Au (JCPDS 04-0784) crystals, and therefore the origin of the peaks could not be discerned. As an alternative to XRD, we used high-resolution transmission electron microscopy (HRTEM) to observe the crystalline phase of the Au-embedded $Ni_xO$ HTLs, and the results are shown in Fig. 2. The top-view HRTEM image in Fig. 2a showed clear lattice fringes occurring throughout the Au nanoislands and the surrounding $Ni_xO$ region, whose spacing of 0.211 nm corresponded to the (200) planes of the NiO crystal, indicating that the $Ni_xO$ phase was indeed crystalline after the 180 °C sintering. To more closely examine the crystallinity of the $Ni_xO$ film under HRTEM, we prepared a cross-section sample with the structure of Si wafer/50 nm Au film/50 nm $Ni_xO$,
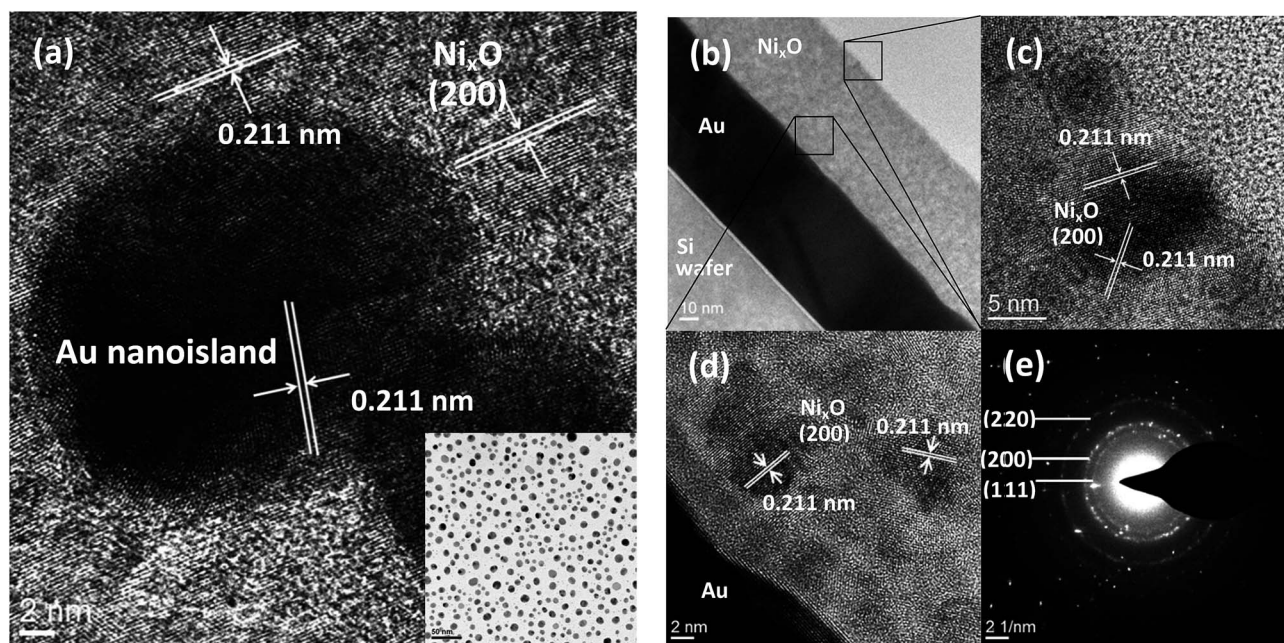


Fig. 2 (a) HRTEM image of the 180 °C-sintered Au nanoisland-embedded $Ni_xO$ film with a low magnitude top-view TEM image in the inset; (b) cross-section TEM image of a 180 °C-sintered Si wafer/50 nm Au film/50 nm $Ni_xO$ film sample; (c) and (d) HRTEM images of the portions marked in (b); (e) selected-area diffraction pattern collected at the center portion of the $Ni_xO$ layer in (b).

16452 | *J. Mater. Chem. A*, 2018, 6, 16450–16457

This journal is © The Royal Society of Chemistry 2018

sintered at 180 °C and cross-sectioned with a focused ion beam (FIB). Fig. 2c and d show the cross-sectional HRTEM images, and Fig. 2e presents a selected-area diffraction pattern collected in the Ni$_x$O region. The cross-sectional HRTEM images showed continuous NiO lattice fringes extending from the Au film/Ni$_x$O interface to the Ni$_x$O top surface, confirming that the Ni$_x$O film was thoroughly crystallized. Additionally, the electron diffraction pattern of the Ni$_x$O film showed three diffraction rings. The d-spacings corresponding to the diffraction rings are 0.25 nm, 0.21 nm, and 0.15 nm, respectively, which in turn correspond to the (111), (200), and (220) planes of NiO. It is worth noting that both forms of embedded Au examined here, nanoislands and flat films, showed the same low-temperature crystallization effect.

Another piece of evidence of complete sintering of the 180 °C-sintered Au-embedded Ni$_x$O film was obtained with XPS (Fig. 3a), where no carbon signal was detected in the bulk of the Ni$_x$O film, indicating that the organic ligands of the sol–gel precursors have been thoroughly removed. This was in sharp contrast to the 180 °C-sintered regular Ni$_x$O film, whose XPS spectrum showed ~40% of carbon content (Fig. 3b). Thermogravimetric analysis (TGA) and differential scanning calorimetry (DSC) analysis also confirmed the significant reduction in the sintering temperature of the Au-embedded Ni$_x$O film, as shown in Fig. S6 (ESI†). The onset temperature for significant weight loss in TGA and the exothermic crystallization peak in DCS were both distinctly lower in the Au-embedded Ni$_x$O samples.

One curious fact regarding the PSC characteristics was that the optimal PCE from the Au-embedded Ni$_x$O HTL (180 °C-sintered) was higher, with higher FF and lower series resistance, than from the regular Ni$_x$O HTL (280 °C-sintered), even though the LSPR absorption of the Au-embedded Ni$_x$O centered at ~550 nm (Fig. S3, ESI†) should have diminished the intensity of the incident light to the perovskite active layer. IPCE measurements (Fig. 1c) revealed that the IPCE of the Au-embedded devices was indeed lower than that of the regular devices in the ~550 nm range, but the difference was small. Moreover, the IPCE of the Au-embedded devices was higher across the rest of the spectrum, where the Au-embedded Ni$_x$O had identical or slightly lower optical transmission than the regular Ni$_x$O. This pointed to the presence of certain enhancement mechanism with the Au-embedded Ni$_x$O. Closer examination with XPS analysis revealed that the chemical composition at the Ni$_x$O surface varied with its annealing temperature, as shown in Fig. 4. Specifically, the O 1s spectra contained a shoulder corresponding to the NiOOH group beside the NiO peak, and the intensity of the NiOOH shoulder intensified by lowering the annealing temperature. This was consistent with the results from water contact angle measurements (Fig. S8, ESI†), where the 180 °C-annealed Ni$_x$O layer showed a lower contact angle than the 280 °C-annealed Ni$_x$O. The NiOOH group has been shown to enhance the performance of the Ni$_x$O HTL in organic solar cells, where its strong dipole facilitates the collection of holes, reducing the series resistance and improving FF.[35] Additionally, the increased hydrophilicity of the low-temperature-annealed Ni$_x$O surface improved the quality of the
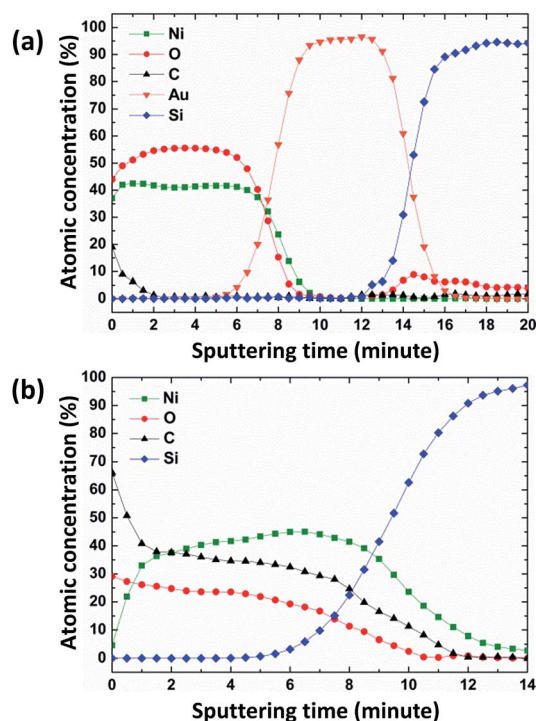


**Fig. 3** XPS depth profiles of 180 °C-sintered sol−gel Ni$_x$O films (a) with an embedded Au film; and (b) without the Au film. The substrates of the samples were Si wafers. Note that the C signals occurring at the beginning of the measurements for both of the samples were generated by surface contamination.
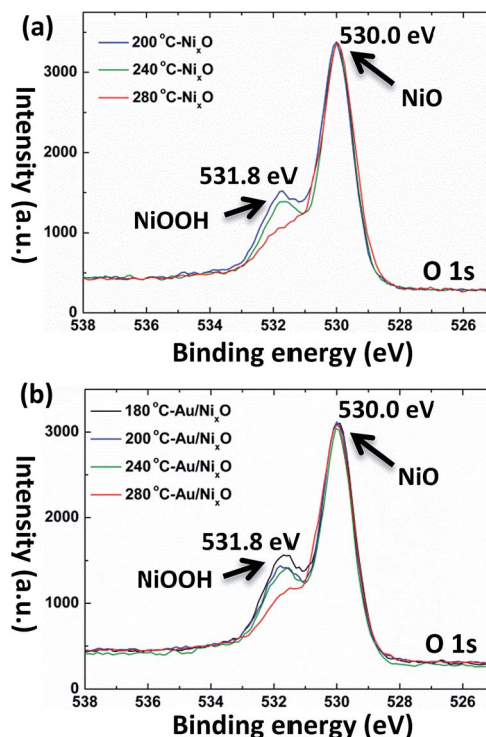


**Fig. 4** O 1s spectra obtained from (a) Ni$_x$O and (b) Au nanoisland-embedded Ni$_x$O film sintered at different temperatures.

This journal is © The Royal Society of Chemistry 2018

*J. Mater. Chem. A*, 2018, **6**, 16450–16457 | **16453**

over-coated perovskite layer, as revealed by SEM in Fig. S9 (ESI†), where the perovskite layer formed on the 180 °C-annealed Ni$_x$O showed larger crystal grains than on the 280 °C-annealed one. Therefore, the enhancement mechanism of the Au-embedded Ni$_x$O was attributable to its low sintering temperatures, which allowed the Ni$_x$O HTL to retain a higher concentration of surface NiOOH groups than did the high-temperature-sintered regular Ni$_x$O, resulting in better HTL function and better film quality of the perovskite layer. This may also account for the slight deterioration of device performance of the 200 °C-sintered Au-embedded devices compared with the 180 °C-sintered ones.

As to the mechanism that enabled the Au-embedded Ni$_x$O film to be fully sintered at low temperatures, we speculated that it followed a similar route to the metal-induced crystallization (MIC) process. The MIC process is widely used to transform
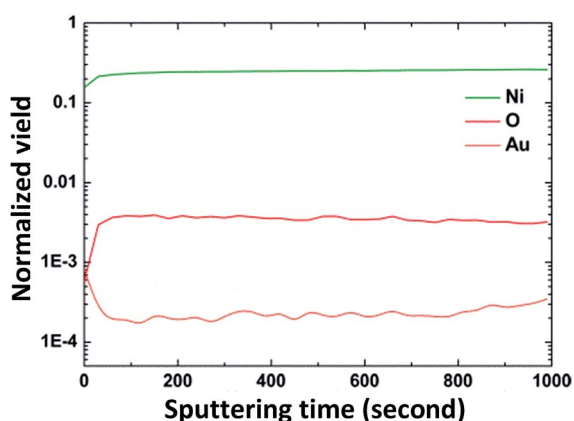
amorphous functional materials to crystalline ones at low temperatures, by physically contacting a metal component (usually a film) with an amorphous material to be transformed.[36–38] The general MIC mechanism involves three steps: (1) an interface layer composed of a monolayer of the metal and the amorphous material is formed at the metal/amorphous material interface; (2) bonding within the amorphous monolayer in the interface layer is weakened by its coordinating interactions with the metal monolayer, allowing the amorphous monolayer to crystallize; (3) the metal monolayer migrates to the front with the amorphous phase to form a new interface layer, and the above steps repeat through the entirety of the amorphous material.[24] To verify whether a similar mechanism occurred in the Au/Ni$_x$O system, we used time-of-flight secondary-ion mass spectrometry (ToF-SIMS), whose high sensitivity enabled accurate determination of trace amounts of elements, to map the Au depth profile starting from the surface of the 180 °C-sintered Si wafer/50 nm Au film/50 nm Ni$_x$O sample. Our rationale was that if a MIC-like mechanism was indeed involved, an Au monolayer would be present at the top surface of the Ni$_x$O film, having migrated there from the Ni$_x$O/Au interface during the MIC process. Fig. 5 presents the Au as well as Ni and O depth profiles determined with ToF-SIMS. It can be clearly seen from the depth profile that the thin layer at the topmost portion of the Ni$_x$O film was Au-rich, indicating that an Au monolayer was indeed present at the top surface. It should be noted that the relative yields of Au, Ni, and O are not directly equal to the ratios of their atomic contents, as the ionization efficiencies of the elements were different in the ToF-SIMS measurements.

Although a MIC-like mechanism appeared to be at play, there was one unique aspect to our observed phenomenon: the Au component not only induced amorphous-to-crystalline



Fig. 5  ToF-SIMS depth profiles of Ni, O, and Au obtained from the 180 °C-sintered Si wafer/50 nm Au film/50 nm Ni$_x$O sample.
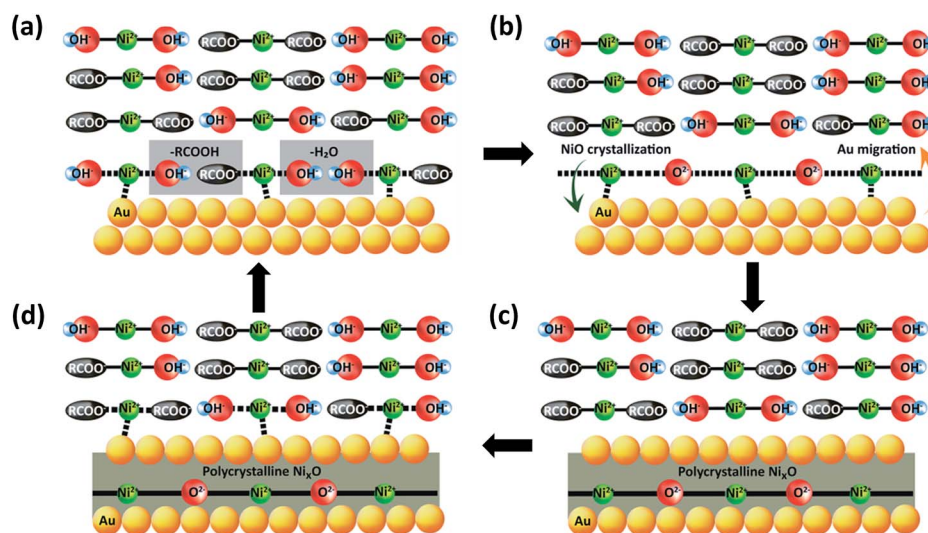


Fig. 6  Schematic illustration of the proposed mechanism of catalytic metal-induced crystallization: (a) weakened bonding (black dashed lines) within the sol–gel precursor at the Au/precursor interface facilitates the removal of organic ligands and the condensation reaction of the precursor; (b) an interface layer consisting of an Au monolayer and an amorphous Ni$_x$O monolayer forms; (c) the amorphous Ni$_x$O monolayer, also with weakened bonding according to the MIC mechanism, crystallizes while the Au monolayer migrates to the new front with the sol–gel phase; (d) an new Au/precursor interface layer forms, repeating the cycle of (a) through (d).

16454 | J. Mater. Chem. A, 2018, 6, 16450–16457

This journal is © The Royal Society of Chemistry 2018

physical transformation of the $Ni_xO$ phase, as occurs in the typical MIC process, but it also catalyzed the chemical reaction of the sol–gel precursors. This phenomenon has not been reported before, and the exact mechanism requires more work to elucidate; but it is conceivable that the bond-weakening effect in a metal/amorphous material interface layer may also occur in a metal/sol–gel precursor interface layer, facilitating the removal of the organic ligands in the precursors and thus freeing the Ni and O atoms to crystallize. A schematic illustration of the above-described catalytic MIC (c-MIC) process is shown in Fig. 6.

In addition to the $NiO_x$/Au system, we verified that the c-MIC mechanism extended to other material systems as well; we observed significant reductions in sintering temperatures in other sol–gel metal oxides embedded with a variety of metals, as summarized in Table 2. For sol–gel $TiO_x$ films, it required ≥400 °C of sintering for the films to begin to crystallize, while embedding them with a Ni, Au, or Pt phase could all reduce the crystallization temperature to ≤350 °C, as shown in the XRD patterns in Fig. 7 as well as the TGA/DSC results in Fig. S7 (ESI†). For sol–gel $SnO_x$ films, the sintering temperature was reduced from ≥325 °C to ≤300 °C with an embedded Ni phase, as shown in the XRD patterns in Fig. S10 (ESI†). For the sol–gel $NiO_x$ films, we found that with Ag instead of Au as the embedded metal, the same sintering temperature reduction (from 280 to 180 °C) was observed, as revealed by the HRTEM image shown in Fig. S11 (ESI†).

**Table 2** The minimum sintering temperatures where extensive crystallinity was observed for several sol–gel systems with a variety of embedded metals

| Metal oxide | Embedded metal for c-MIC | Minimum sintering temperature for crystallization (°C) |
|---|---|---|
| $Ni_xO$ | None | 280 |
|  | Au | 180 |
|  | Ag | 180 |
| $TiO_x$ | None | 400 |
|  | Ni | 350 |
|  | Au | 350 |
|  | Pt | 350 |
| $SnO_x$ | None | 325 |
|  | Ni | 300 |

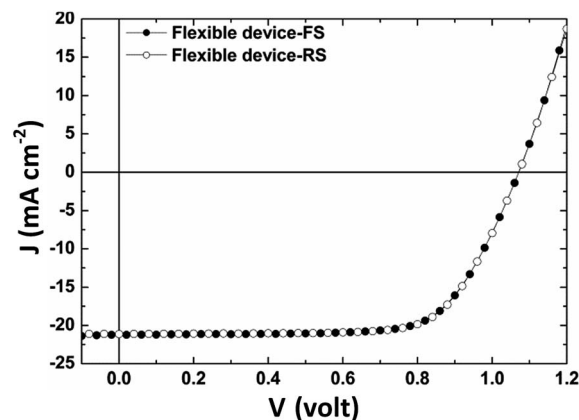**Fig. 8** $J$–$V$ characteristics of a flexible PSC device based on a PEN substrate.

Utilizing the 180 °C-sintered Au nanoislandembedded $Ni_xO$ HTL, we demonstrated fabrication of the plastic-based flexible PSC device. Fig. 8 presents the $J$–$V$ characteristics, both FS and RS, of the flexible PSC devices based on poly(ethylene naphthalate) (PEN) substrates. The flexible devices achieved average and champion PCE values of 14.0 and 15.9%, respectively, without detectable $J$–$V$ hysteresis (a PCE histogram of 9 flexible PSCs is shown in Fig. S12, ESI†). The PCE of the flexible devices was lower than that of their rigid counterparts primarily because of the lower optical transparency and higher electrical resistance of the ITO films on the PEN substrates. The continuous power output was also measured for the flexible as well as the rigid champion devices by fixing the applied voltage at the maximum-PCE value while monitoring the current density changing with time, and the results are shown in Fig. S13a (ESI†). Both the flexible and rigid devices exhibited steady current density (18.2 and 21.3 mA cm$^{-2}$, respectively) near their respective $J$–$V$ scan maxima, resulting in steady PCE (15.3 and 18.7%, respectively) that were very close to $J$–$V$ scan values (15.9 and 19.0%). This further confirmed the hysteresis-free nature of the devices. The stability of the PSC devices was evaluated under an accelerated aging condition of 65 °C and 65% relative humidity, and the results are presented in Fig. S13b (ESI†). Thanks to the stable nature and excellent quality of the
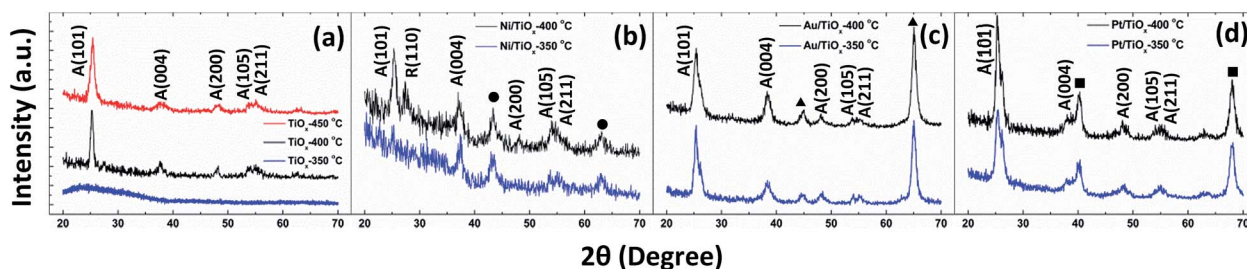
**Fig. 7** GIXRD patterns of $TiO_2$ films sintered at different temperatures with different embedded metal films: (a) none, (b) Ni, (c) Au, and (d) Pt. The labels "A" and "R" denote anatase and rutile phases of crystalline $TiO_2$, respectively. The diffraction peaks resulting from the embedded phases are also labelled ● for NiO, ▲ for Au, and ■ for Pt.

Ni$_x$O HTL, the PSC devices upon encapsulation showed excellent stability, retaining over 90% of its initial PCE value after 1200 hours of the accelerated aging test. This represented a significant improvement over many other types of HTL materials as well as the Ni$_x$O HTL fabricated with other methods, where the PCE drop was typically much more rapid under milder testing conditions (*i.e.* lower temperatures and/or lower R.H.).[39–41] In terms of mechanical flexibility, the flexible devices were able to retain 93% of their initial PCE value after 1000 times of bending at a radius of curvature of 1.35 cm (Fig. S13c, ESI†).

## Conclusions

In summary, a new phenomenon related to the metal-induced crystallization mechanism was discovered, where a sol–gel precursor film in contact with a metal phase exhibited greatly reduced sintering temperature *via* the catalytic action of the metal/precursor interface layer. Specifically, a Ni$_x$O sol–gel precursor film embedded with Au nanoislands underwent a complete reaction and extensive crystallization at 180 °C, as opposed to the 280 °C required to fully sinter a Ni$_x$O sol–gel precursor film without the embedded Au phase. Depth-profiling elemental analysis revealed that an Au-containing interface layer migrated through the entirety of the Ni$_x$O film during sintering, similar to the MIC process. The low sintering temperatures of the Au-embedded Ni$_x$O film permitted its incorporation into flexible as well as rigid perovskite solar cell devices as a hole-transporting layer, achieving PCEs of up to 15.9 and 19.0% from the flexible and rigid devices, respectively, with excellent stability under accelerated aging conditions. Moreover, the low sintering temperature of the Au-embedded Ni$_x$O HTL allowed it to retain a higher concentration of surface NiOOH groups, which enhanced hole-collection at the Ni$_x$O surface and improved the quality of the over-coated perovskite film, resulting in superior PSC performance. More importantly, the generality of the c-MIC mechanism was demonstrated with several sol–gel material systems, including TiO$_x$ with embedded Ni, Au, or Pt; SnO$_x$ with embedded Ni; and NiO$_x$ with embedded Ag instead of Au. Our findings provide a practical route for low-temperature fabrication of high-quality oxide functional films from solution-based sol–gel processes, which will be valuable to a wide variety of energy applications in addition to thin film solar cells.

## Conflicts of interest

There are no conflicts of interest to declare.

## Acknowledgements

## References

1 X. Yu, T. J. Marks and A. Facchetti, *Nat. Mater.*, 2016, **15**, 383–396.

2 W. Chen, Y. Wu, Y. Yue, J. Liu, W. Zhang, X. Yang, H. Chen, E. Bi, I. Ashraful, M. Grätzel and L. Han, *Science*, 2015, **350**, 944–948.

3 E. H. Anaraki, A. Kermanpur, L. Steier, K. Domanski, T. Matsui, W. Tress, M. Saliba, A. Abate, M. Grätzel, A. Haqfeldt and J.-P. Correa-Baena, *Energy Environ. Sci.*, 2016, **9**, 3128.

4 L. M. Daniels, S. N. Savvin, M. J. Pitcher, M. S. Dyer, J. B. Claridge, S. Ling, B. Slater, F. Corá, J. Alaria and M. J. Rosseinsky, *Energy Environ. Sci.*, 2017, **10**, 1917.

5 P. Jood, R. J. Mehta, Y. Zhang, G. Peleckis, X. Wang, R. W. Siegel, T. B. Tasciuc, S. X. Dou and G. Ramanath, *Nano Lett.*, 2011, **11**, 4337–4342.

6 C. Wu, F. Feng and Y. Xie, *Chem. Soc. Rev.*, 2013, **42**, 5157.

7 X. Liu, J.-Q. Huang, Q. Zhang and L. Mai, *Adv. Mater.*, 2017, **29**, 1601759.

8 J. Wang, H. Tang, L. Zhang, H. Ren, R. Yu, Q. Jin, J. Qi, D. Mao, M. Yang, Y. Wang, P. Liu, Y. Zhang, Y. Wen, L. Gu, G. Ma, Z. Su, Z. Tang, H. Zhao and D. Wang, *Nat. Energy*, 2016, **1**, 16050.

9 D. Kundu, R. Black, E. J. Berg and L. F. Nazar, *Energy Environ. Sci.*, 2015, **8**, 1292.

10 S. Boukhalfa, K. Evanoff and G. Yushin, *Energy Environ. Sci.*, 2012, **5**, 6872.

11 X. Lu, D. Zheng, T. Zhai, Z. Liu, Y. Huang, S. Xiea and Y. Tong, *Energy Environ. Sci.*, 2011, **4**, 2915.

12 R. L. Z. Hoye, M. R. Chua, K. P. Musselman, G. Li, M.-L. Lai, Z.-K. Tan, N. C. Greenham, J. L. MacManus-Driscoll, R. H. Friend and D. Credgington, *Adv. Mater.*, 2015, **27**, 1414–1419.

13 X. Dai, Z. Zhang, Y. Jin, Y. Niu, H. Cao, X. Liang, L. Chen, J. Wang and X. Peng, *Nature*, 2014, **515**, 96.

14 M.-G. Kim, M. G. Kanatzidis, A. Facchetti and T. J. Marks, *Nat. Mater.*, 2011, **10**, 382–388.

15 S. Ju, A. Facchetti, Y. Xuan, J. Liu, F. Ishikawa, P. Ye, C. Zhou, T. J. Marks and D. B. Janes, *Nat. Nanotechnol.*, 2007, **2**, 378–384.

16 X. Yin, P. Chen, M. Que, Y. Xing, W. Que, C. Niu and J. Shao, *ACS Nano*, 2016, **10**, 3630–3636.

17 S. Bai, M. Cao, Y. Jin, X. Dai, X. Liang, Z. Ye, M. Li, J. Cheng, X. Xiao, Z. Wu, Z. Xia, B. Sun, E. Wang, Y. Mo, F. Gao and F. Zhang, *Adv. Energy Mater.*, 2014, **4**, 1301460.

18 J. W. Jung, C.-C. Chueh and A. K.-Y. Jen, *Adv. Mater.*, 2015, **27**, 7874–7880.

19 T. J. Konno and R. Sinclair, *Mater. Sci. Eng., A*, 1994, **179/180**, 426–432.

20 J. Jang, J. Y. Oh, S. K. Kim, Y. J. Choi, S. Y. Yoon and C. O. Kim, *Nature*, 1998, **395**, 481–483.

21 G. Radnoczi, A. Robertsson, H. T. G. Hentzell, S. F. Gong and M.-A. Hasan, *J. Appl. Phys.*, 1991, **69**, 6394–6399.

22 S. Y. Yoon, K. H. Kim, C. O. Kim, J. Y. Oh and J. Jang, *J. Appl. Phys.*, 1997, **82**, 5865–5867.

23  S. Y. Yoon, S. J. Park, K. H. Kim and J. Jang, *Thin Solid Films*, 2001, **383**, 34–38.

24  Z. M. Wang, J. Y. Wang, L. P. H. Jeurgens and E. J. Mittemeijer, *Phys. Rev. B: Condens. Matter Mater. Phys.*, 2008, **77**, 045424.

25  M. D. Irwin, D. B. Buchholz, A. W. Hains, R. P. H. Chang and T. J. Marks, *Proc. Natl. Acad. Sci. U. S. A.*, 2008, **105**, 2783–2787.

26  K. X. Steirer, J. P. Chesin, N. E. Widjonarko, J. J. Berry, A. Miedaner, D. S. Ginley and D. C. Olson, *Org. Electron.*, 2010, **11**, 1414.

27  N. E. Widjonarko, E. L. Ratcliff, C. L. Perkins, A. K. Sigdel, A. Zakutayev, P. F. Ndione, D. T. Gillaspie, D. S. Ginley, D. C. Olson and J. J. Berry, *Thin Solid Films*, 2012, **520**, 3813–3818.

28  J. J. Berry, N. E. Widjonarko, B. A. Bailey, A. K. Sigdel, D. S. Ginley and D. C. Olson, *IEEE J. Sel. Top. Quantum Electron.*, 2010, **16**, 1649.

29  K. X. Steirer, P. F. Ndione, N. E. Widjonarko, M. T. Lloyd, J. Meyer, E. L. Ratcliff, A. Kahn, N. E. Armstrong, C. J. Curtis, D. S. Ginley, J. J. Berry and D. C. Olson, *Adv. Energy Mater.*, 2011, **1**, 813–820.

30  M. D. Irwin, J. D. Servaites, D. B. Buchholz, B. J. Leever, J. Liu, J. D. Emery, M. Zhang, J.-H. Song, M. F. Durstock, A. J. Freeman, M. J. Bedzyk, M. C. Hersam, R. P. H. Chang, M. A. Ratner and T. J. Marks, *Chem. Mater.*, 2011, **23**, 2218–2226.

31  J.-Y. Jeng, K.-C. Chen, T.-Y. Chiang, P.-Y. Lin, T.-D. Tsai, Y.-C. Chang, T.-F. Guo, P. Chen, T.-C. Wen and Y.-J. Hsu, *Adv. Mater.*, 2014, **26**, 4107–4113.

32  K. X. Steirer, R. E. Richards, A. K. Sigdel, A. Garcia, P. F. Ndione, S. Hammond, D. Baker, E. L. Ratcliff, C. Curtis, T. Furtak, D. S. Ginley, D. C. Olson, N. R. Armstrong and J. J. Berry, *J. Mater. Chem. A*, 2015, **3**, 10949.

33  Y. Shao, Z. Xiao, C. Bi, Y. Yuan and J. Huang, *Nat. Commun.*, 2014, **5**, 5784.

34  W. Zhou, J. Zhen, Q. Liu, Z. Fang, D. Li, P. Zhou, T. Chen and S. Yang, *J. Mater. Chem. A*, 2017, **5**, 1724–1733.

35  E. L. Ratcliff, J. Meyer, K. X. Steirer, A. Garcia, J. J. Berry, D. S. Ginley, D. C. Olson, A. Kahn and N. R. Armstrong, *Chem. Mater.*, 2011, **23**, 4988–5000.

36  C. Yang, Y. Hirose, S. Nakao, N. L. H. Hoang and T. Hasegawa, *Appl. Phys. Lett.*, 2012, **101**, 052101.

37  C. Yang, Y. Hirose, S. Nakao and T. Hasegawa, *Thin Solid Films*, 2014, **553**, 17–20.

38  A. Y. Hwang, S. T. Kim, H. Ji, Y. Shin and J. K. Jeong, *Appl. Phys. Lett.*, 2016, **108**, 152111.

39  Z. H. Bakr, Q. Wali, A. Fakharuddin, L. Schmidt-Mende, T. M. Brown and R. Jose, *Nano Energy*, 2017, **34**, 271–305.

40  M. Cheng, Y. Li, M. Safdari, C. Chen, P. Liu, L. Kloo and L. Sun, *Adv. Energy Mater.*, 2017, **7**, 1602556.

41  X. Yan, J. Zheng, L. Zheng, G. Lin, H. Lin, G. Chen, B. Du and F. Zhang, *Mater. Res. Bull.*, 2018, **103**, 150–157.

This journal is © The Royal Society of Chemistry 2018

*J. Mater. Chem. A*, 2018, **6**, 16450–16457 | **16457**